Mid-infrared reflectance spectroscopy of aubrite components

Andreas MORLOK [1]*, Iris WEBER[1], Aleksandra N. STOJIC[1], Martin SOHN[2], Addi BISCHOFF [1],
Dayl MARTIN [3], Harald HIESINGER[1], and Joern HELBERT[4]

[1]Institut für Planetologie, Westfälische Wilhelms Universität, Münster, Wilhelm-Klemm-Str. 10, Münster 48149, Germany
[2]Hochschule Emden/Leer, Constantiaplatz 4, Emden 26723, Germany
[3]European Space Agency, Fermi Avenue, Harwell Campus, Didcot, Oxfordshire OX11 0FD, UK
[4]Institute for Planetary Research, DLR, Rutherfordstrasse 2, Berlin 12489, Germany
*Corresponding author. E-mail: morlokan@uni-muenster.de

Abstract–Aubrites Peña Blanca Spring and Norton County were studied in the mid-infrared reflectance as part of a database for the MERTIS (Mercury Radiometer and Thermal Infrared Spectrometer) instrument on the ESA/JAXA BepiColombo mission to Mercury. Spectra of bulk powder size fractions from Peña Blanca Spring show enstatite Reststrahlen bands (RB) at 9 μm, 9.3 μm, 9.9 μm, 10.4 μm, and 11.6 μm. The transparency feature (TF) is at 12.7 μm, the Christiansen feature (CF) at 8.1–8.4 μm. Micro-FTIR of spots with enstatite composition in Norton County and Peña Blanca Spring shows four types: Types I and II are similar to the bulk powder spectra but vary in band shape and probably display axis orientation. Type III has characteristic strong RB at 9.2 μm, 10.4 μm, and 10.5 μm, and at 11.3 μm. Type IV is characterized by a strong RB at 10.8−11.1 μm. Types III and IV could show signs of incipient shock metamorphism. Bulk results of this study confirm earlier spectral studies of aubrites that indicate a high degree of homogeneity and probably make the results of this study representative for spectral studies of an aubrite parent body. Spectral types I and II occur in all mineralogical settings (mineral clasts, matrix, melt, fragments in melt vein), while spectral type III was only observed among the clasts, and type IV in the melt. Comparison with surface spectra of Mercury does not obtain a suitable fit, only type IV spectra from quenched impact glass show similarity, in particular the 11 μm feature. Results of this study will be available upon request or via the IRIS database (Münster) and the Berlin Emissivity Database (BED).

INTRODUCTION

The ESA/JAXA joint mission BepiColombo is dedicated to exploring the innermost solar system planet, Mercury. The spacecraft BepiColombo, which was launched successfully in October 2018, includes a mid-infrared spectrometer (MERTIS—Mercury Radiometer and Thermal Infrared Spectrometer) that can be used to map the surface of Mercury from Hermean orbit in the 7–14 μm spectral range, with a spatial resolution of ~500 m (Helbert et al. 2007; Benkhoff et al. 2010; Hiesinger et al. 2010). Generally though, to interpret and evaluate the spectral data obtained from such space missions, the collected data must be compared with laboratory spectral data in the mid-infrared range from planetary crust-forming rocks and minerals, as well as from meteorites.

While meteorite samples definitely associated with Mercury are not available in our collections, several meteorite types have been suggested as potentially originating from the innermost planet (Gladman and Coffey 2007; Vaughan and Head 2014). Among them are the ungrouped achondrite NWA7325 (Weber et al. 2016), angrites (Blewett and Burbine 2007; Kuehner and Irving 2007), and aubrites or related materials (Love and Keil 1995; McCoy and Bullock 2015; Udry et al. 2019).

Aubrites are differentiated meteorites (achondrites) and are typically brecciated. They are characterized by their mineralogy indicating that they formed under

highly reducing conditions. The petrographic composition of aubrites, which is dominated by coarse-grained Fe-poor enstatite; some plagioclase; and minor forsterite, diopside, metal, and sulfides (Mittlefehldt et al. 1998; Barrat et al. 2016), suggests they formed under highly reducing crystallization conditions with a very low surface oxygen fugacity (fO_2) less than -2.3 of the iron–wuestite buffer (IW; Zolotov et al. 2013; McCubbin et al. 2017), making them a promising natural analog for Mercury material.

Recently, Udry et al. (2019) reclassified particular aubrites as enstatite chondrite impact melts that could also serve as an analog for the surface of Mercury regarding their petrography, fO_2, and iron-deficient chemical composition.

The MESSENGER mission revealed a diverse chemical and petrographic composition of the Hermean surface likely predominantly consisting of plagioclase, forsterite, enstatite, and diopside, with quartz and sulfides as minor constituents (e.g., Weider et al. 2012, 2015; Namur and Charlier 2017; Vander Kaaden et al. 2017). Results from an Earth-based mid-infrared study by Sprague et al. (2009) led to a petrographic surface model comprising various abundances of olivine, ortho- and clinopyroxene, feldspars, and rutile, with additional perovskite and garnet.

In addition, amorphous components probably also are an important part of the surface material. Based on Hapke modeling, Warrell et al. (2010) estimated a glass content of 20–45% for the regolith.

Similar petrological experiments by Namur et al. (2016) and Namur and Charlier (2017) allow a glassy component of at least 20 wt%.

However, so far spectral studies of aubrites are rare. These studies have mostly been limited to studies in the visible and near-infrared range (Cloutis and Gaffey 1993; Burbine et al. 2002; Izawa et al. 2013; Cloutis et al. 2016) or, where mid-infrared range studies are available, they are limited to transmission studies, which are not suitable for planetary surface studies (Sandford 1984; Morlok et al. 2012, 2014). Exceptions for the mid-infrared reflection range are a spectrum of ALH84007 (Salisbury et al. 1991) and the study of Markus et al. (2018), who performed a reflectance study of bulk. They found that the spectra reflect a high enstatite content and are dominated by enstatite features.

In order to accurately evaluate and interpret the data obtained of a planetary surface such as Mercury by MERTIS, the available data need to be expanded. Surface regolith is a porous material consisting of various grain sizes, which makes obtaining size-dependent spectra necessary. Furthermore, while the aubrites' spectra so far show the dominance of enstatite

features (Salisbury et al. 1991; Markus et al. 2018), they still are a mixture of various minerals (Love and Keil 1995; McCoy and Bullock 2015), and possibly phases formed, for example, during impacts as observed for other meteorites (e.g., ordinary chondrites; Morlok et al. 2017b). So bulk spectral studies of laboratory samples are only part of the picture—there could be variations in the bulk material which are small or minor in the available samples, but could be more prominent in other parts of the parent body not "sampled" by the meteorite (also compare Morlok et al. 2017b).

Therefore, the aim of this study is to provide bulk reflectance spectra of size fractions of analog material in the form of the aubrites. We present bulk sample measurements of several grain size fractions (0–25 µm, 25–63 µm, 63–125 µm, 125–250 µm). Changes in grain sizes affect spectral features in the mid-infrared range, and the effects occurring at smaller grain sizes are particularly important because previous studies of the surface regolith on Mercury indicated a high abundance of grains smaller than 25 µm in size (e.g., Sprague et al. 2007). These effects include, for example, a decrease in the intensity of Reststrahlen bands (RB) and the occurrence of the transparency feature (TF) in the finest size fraction (<~25 µm; e.g., Salisbury and Wald 1992; Clark 1999).

In addition, we provide in situ reflectance spectra from designated areas obtained by micro-FTIR in addition to bulk spectral analyses, which will enable us to investigate small-scale peculiarities in the spectral data that could otherwise be missed in bulk spectral measurements. In particular, the effect of the degree of shock metamorphism on the IR spectra is of interest. In this respect, the Norton County aubrite displays signs of heavy impact shock in the form of abundant melt veins. The spectral identification and characterization of these veins may help to mark and characterize textures associated with the veins as areas that probably underwent various degrees of impact processing (e.g., Morlok et al. 2017b) on the parent bodies. These veins are typically small in diameter or are parts of a mixture of various lithologies. Thus, in situ studies using infrared microscopy (micro-FTIR) are necessary to obtain reflectance spectra of these samples.

We focus especially on the mid-infrared characteristics of two particular aubrites, Peña Blanca Spring and Norton County. However, carbonates as potential terrestrial alteration phases were observed in Norton County (Okada et al. 1988). While both meteorites are observed falls, Peña Blanca Spring managed to fall into a swimming pool in 1946 (Lonsdale 1947; Lodders et al. 1993). Norton County fell in 1948 (Okada and Keil 1981), so storage under

Fig. 1. Optical images of thin sections. Squares show areas for micro-FTIR analyses. Black/white squares: single crystals; dotted black/white squares: breccia areas; white squares: shock-darkened area; dotted white squares:melt veins. a) Optical image of polished thin section from Peña Blanca Spring PL92044. Large crystals are embedded in brecciated areas of finer material. Top: normal light; bottom: with crossed polarizers. Enlarged: mineral grain with analyses Peña Blanca Spring, which shows high interference colors. b) Norton County PL14026 shows smaller fragments of single crystals and shock-darkened materials (SD) in dark melt vein. In addition, two larger fragments are presented. c and d) Norton County PL14026 also has areas of melt vein with embedded fragments of large grains with shock-darkened areas. Similar larger fragments also show signs of shock darkening (d). (Color figure can be viewed at wileyonlinelibrary.com.)

not entirely modern standards may have potentially resulted in terrestrial weathering.

Overall, our approach of applying reflectance spectroscopy on powdered and polished meteorite samples from two selected aubrites will add to the database of spectral data collected from diverse samples of this meteorite class. This comprehensive database can thereby be used in applications for remote sensing of planetary surfaces and asteroids.

MATERIALS AND METHODS

Samples and Preparation

In this study, two types of aubrite materials from Peña Blanca Spring and Norton County were studied: powdered bulk rocks and thin sections. We studied bulk powder because it likely represents the fine-grained, porous regolith-like surface material of an aubrite parent body, while the thin sections were made to allow for investigating the details of the aubrite material, such as minor minerals or components showing various effects of shock metamorphism like melt veins. These details might be difficult to investigate in bulk rock samples or powdered bulk rock samples, which contain all these different phases mixed together (Morlok et al. 2017b). Regarding the thin sections for the Peña Blanca Spring and Norton County samples, we investigated the thin sections PL92044 and PL 14026/PL14027, respectively, from the collection at the Institut für Planetologie.

Peña Blanca Spring (Fig. 1a) is a well-preserved fall from 1946 that provided ample material (70 kg). The total mass of the meteorite and its short exposure to terrestrial weathering makes it an ideal material for the bulk powder analyses. Five grams were used and sieved in order to produce the required grain size fractions. Norton County (Figs. 1b and 1c) is also a fall (1948) that provided over a ton of material. Abundant melt veins in the Norton County aubrite allow for their detailed analyses with micro-FTIR.

For "bulk fractions," powdered bulk sample material was sieved from sample material ground in steel and agate mortars. The powder was dry sieved using an automatic Retsch Tap Sieve for 1 hour into four size fractions: 0–25 μm, 25–63 μm, 63–125 μm, and 125–250 μm. In order to remove clinging fines, the larger two fractions were cleaned in acetone.

Metal grains (kamacite) occurring in the aubrites pose a challenge in grinding samples. They are difficult to break into smaller particles and tend to flatten under pressure. However, metal/kamacite content in aubrites is very small (<0.3 vol%; Watters and Prinz, 1979). Therefore, we consider any influence of the grains, for example, on intensities as minor.

For the micro-FTIR measurements, polished thin sections were prepared from samples, which were also used for the analyses of the different size fractions.

Optical Studies

Polished thin sections of aubrites from the collection of the Institut für Planetologie (Münster) were examined using a ZEISS polarizing microscope (Axiophot) in order to select specific samples for detailed studies. From these samples, overview images were prepared using a KEYENCE Digital Microscope VHX-500F (Figs. 1a–d and 2a-f). A petrographic characterization of representative areas of the bulk sample material was performed on thin sections in transmitted and reflected light.

Electron Microprobe (EMPA) Studies

Detailed quantitative analyses of the thin sections were made with a JEOL JXA-8530F Hyperprobe electron probe micro analyzer (EPMA) equipped with four wavelength dispersive spectrometers and operating at an excitation voltage of 15 kV and a beam current of 15 nA. Corrections for matrix effect were made using the Φρ(z) procedure of Armstrong (1991). Natural and synthetic standards of well-known compositions were used. In some cases, a JEOL JSM-6610LV scanning electron microscope (SEM) was used for additional quantitative analyses. All scanning electron microscope measurements were carried out at an accelerating voltage of 20 kV.

(a)

(b)
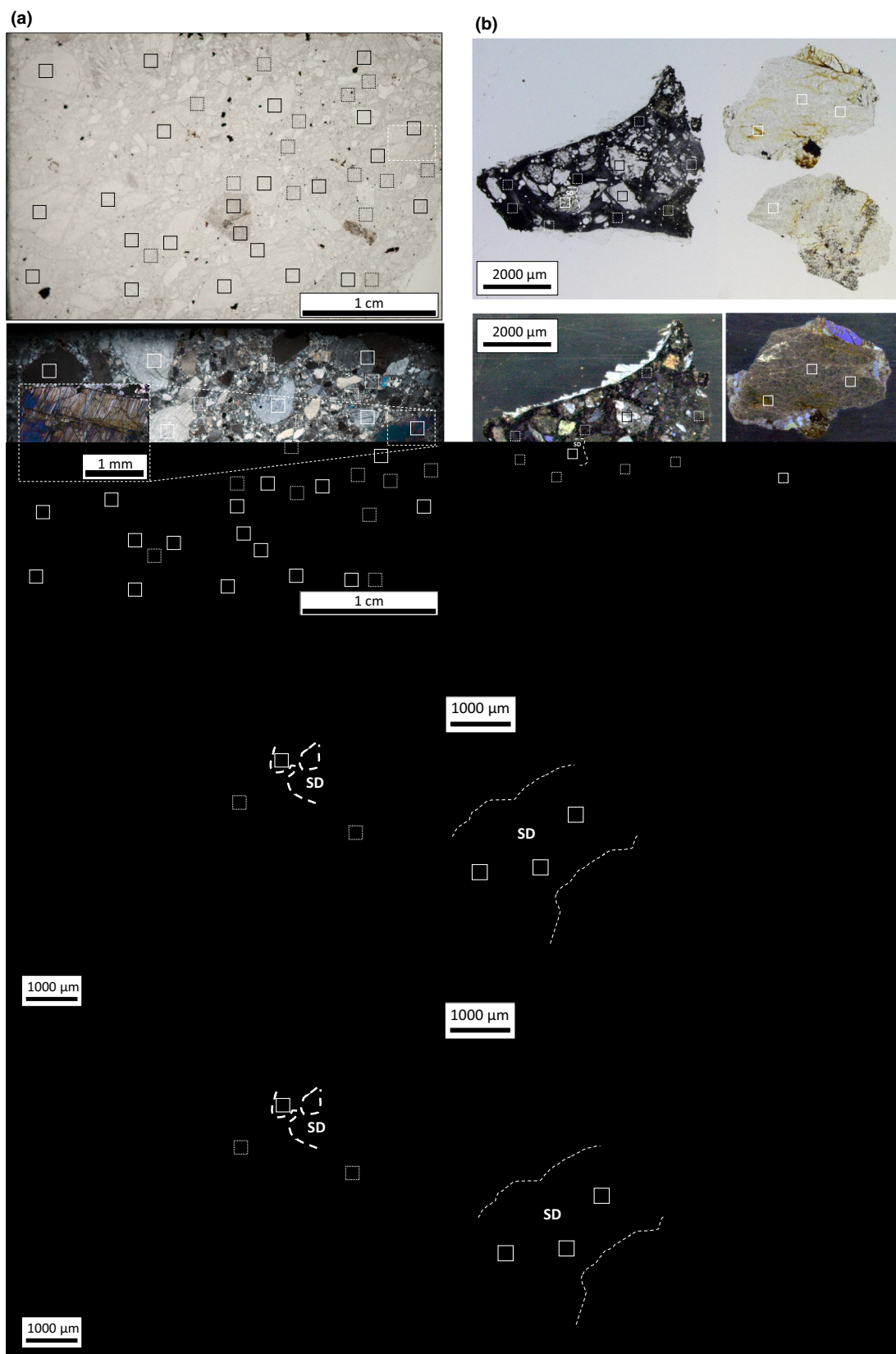
Diffuse Reflectance Powder FTIR

For subsequent diffuse reflectance analyses, each size fraction was placed in aluminum sample cups with 1 cm diameter. Prior to the actual spectral measurement, the powder surface was flattened using a spatula similar to the procedure described by Mustard and Hays (1997).

We used a Bruker Vertex 70v infrared system with an MCT detector at the IRIS (Infrared and Raman for Interplanetary Spectroscopy) laboratory at the Institut für Planetologie (Münster). Analyses were performed in the mid-infrared range from 2.5 to 18 μm under low pressure (10^{-3} bar). For a high signal-to-noise ratio, we accumulated 512 scans for each size fraction and used a diffuse gold standard (INFRAGOLD^{TM}) for background calibration. In order to simulate various observational geometries of an orbiter, we obtained analyses in a variable geometry stage (Bruker A513). The spectral resolution is 0.02 μm. The data presented in this study were obtained at 20° incidence (i) and 30° emergence angle (e) (Fig. 3). These low incidence/emergence angles are best suited to fit remote sensing data (Moroz and Schade 2011).

To compare them with planetary remote sensing data, reflectance spectra as obtained in this study have to be transformed into emission spectra. Emission and reflectance data are related by Kirchhoff's law via ε = 1 – R (R = reflectance, ε = emission; nicodemus 1965). This relation works well for comparing directional emissivity and directional hemispherical reflectance (Hapke 1993; Salisbury 1993), but in order to be able to use Kirchoff's law for a direct comparison of directional emissivity with diffuse reflectance spectra, the diffusely reflected light during spectral measurements has to be collected ideally completely by a hemispherical mirror (e.g., Thomson and Salisbury 1993). In this study, a bidirectional, variable mirror setup was used. This system allows for omitting the use of a hemisphere mirror (which would be problematic in our analytical setup) by integrating the missing directions of the reflected light. This approximation must be kept in mind when comparing the results with emission data in a quantitative manner (Salisbury et al. 1991; Christensen et al. 2001).

Reflectance studies on these samples should provide three interesting spectral features. First, characteristic spectral features to be expected in the mid-infrared range are the RB. The RB are vibrational modes of molecules, essentially the spectral fingerprint of the analyzed phases, and they are strongest for larger grains due to their larger surfaces (e.g., Clark 1999). In the reflectance spectra presented here, they are identified as the local maxima ("peaks"). Another feature is the CF, a reflectance minimum. It is usually the easiest feature to identify in most spectra, and it occurs at the wavelength where the index of refraction and that of the surrounding medium are identical (e.g., Clark 1999). The third important spectral feature of note is the TF. The TF is the result of volume scattering at wavelengths of low absorbance, and it is usually visible in spectra of the finest grain size fraction (0–25 μm in this study; Salisbury 1993; Mustard and Hays 1997).

The spectra for this study were made under room temperature conditions. Application of the results for remote sensing of planetary surfaces will have to take thermal gradients into account. The surface of, for example, Mercury shows a range from −180 °C to 430 °C (Rothery et al. 2020). Especially high temperature will affect spectral features (band shape and position), but also the high vacuum conditions (e.g., Donaldson-Hanna et al. 2012; Helbert et al. 2013; Ferrari et al. 2020). The aim of this study is to provide the basic mid-infrared spectral properties of the investigated material. Detailed high temperature and low-vacuum analyses will be part of a later study.

The spectra presented in this study are available upon request or will be accessible via the IRIS online database at the Institut für Planetologie in Münster (http://www.unimuenster.de/Planetology/en/ifp/ausstattung/iris_spectra_database.html), and the Berlin Emissivity Database (BED).

This research utilizes spectra for aubrite ALH 78113 (bir1ar001c and bir1ar001b) acquired by Andrew S. Rivkin with the NASA RELAB facility at Brown University.

Micro-FTIR

We used a Bruker Hyperion 2000 IR microscope attached to the external port of a Bruker Vertex 70v at the Hochschule Emden/Leer. For the analyses of crystal grains and brecciated areas in Peña Blanca Spring, a 1000 × 1000 μm sized aperture was applied to obtain in situ analyses of features in reflectance on polished thin sections. Before the analyses, we took test measurements to ensure that analyses do not contain stray signals from specimen holder and resin. One hundred and twenty-eight scans were added for each spectrum. For the more fine-grained Norton County samples, a smaller aperture of 256 × 256 μm with 256 scans was applied. A gold mirror was used for background calibration. The analyses were made in the range from 2–15 μm at a spectral resolution of 0.02 μm (Fig. 4).

Since micro-FTIR spectra were obtained from flat, polished surfaces, they do not contain grain size-related features. So the important TF is lacking in these data. Still, the spectra are of use for comparison, for example,
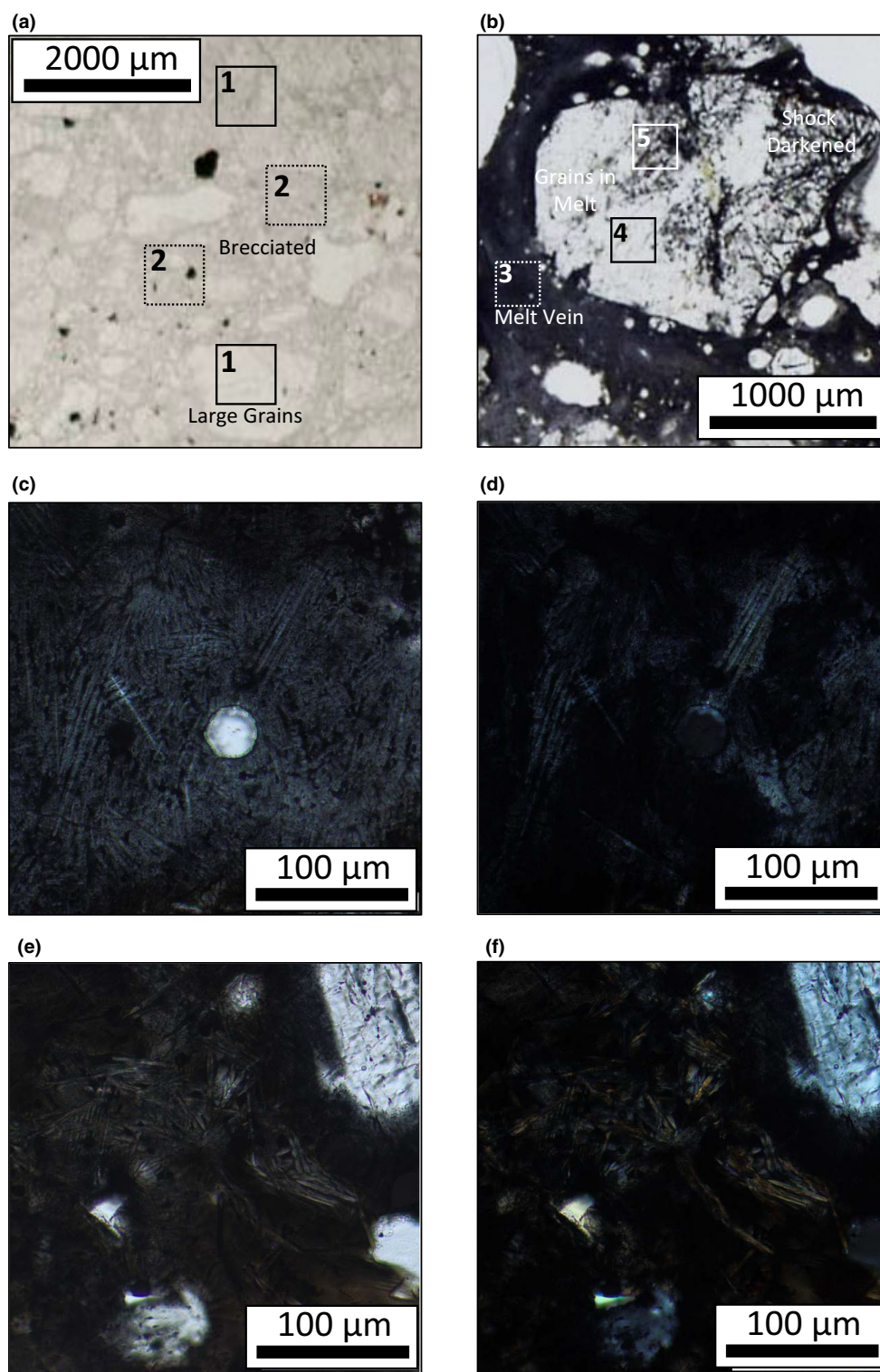
Fig. 2. a and b) Optical images of enlarged parts form the Peña Blanca Spring and Norton County samples in order to illustrate the characteristics of the five components found in the samples. [1] Large, single grains; [2] brecciated areas consisting of several, smaller and finer particles; [3] veins of shock-melted material; [4] larger grains embedded in the melt; [5] darkened areas presumably of shock-darkened origin. c–f) Enlarged representative parts of the melt vein in Norton County, which show needle and skeletal structures in the recrystallized melt; (c and e) are in plain polarized light for PL14026 and PL14027, respectively, (d and f) are the same areas with crossed polarizers. (Color figure can be viewed at wileyonlinelibrary.com.)
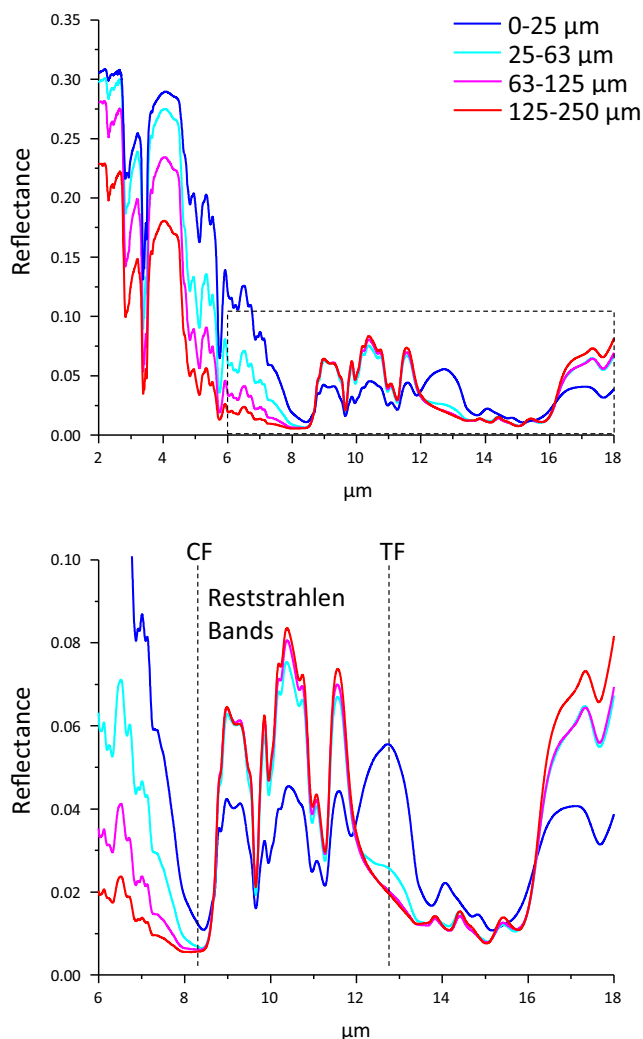
Fig. 3. FTIR spectra of bulk powdered size fractions of Peña Blanca Spring. Top image: spectra over whole recorded range from 2 μm to 18 μm; bottom: enlarged box from top image covering the range from 6 to 18 μm. Finest size fraction (0–25 μm) is in dark blue, 25–63 μm in light blue, 63–125 μm in pink, and 125–250 μm in red. (Color figure can be viewed at wileyonlinelibrary.com.)

to remote sensing data. They allow identifying CF and RB features of potentially important lithologies, which are only minor in the meteorite samples, but more widespread in the observed bodies.

RESULTS

Optical Images

The Peña Blanca Spring breccia (Fig. 1a, top) shows abundant large crystal clasts of up to ~1 cm with accessory anhedral olivine grains and minor opaque phases set in a fine-grained clastic matrix. The grains
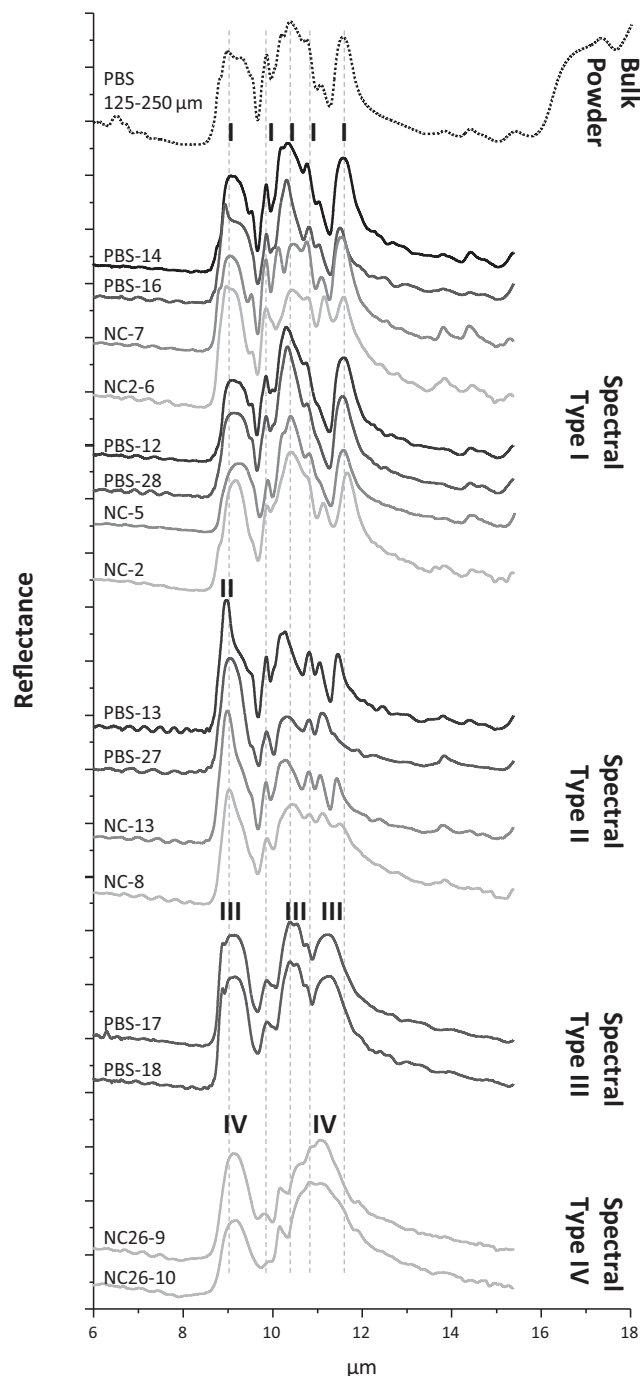
Fig. 4. Comparison of micro-FTIR spectra of groups types I–IV with the 125–250 μm spectrum of the bulk Peña Blanca Spring data (Fig. 3). For types I and II, only representative spectra are presented; types III and IV are the two available spectra for the whole group. Horizontal lines denote important spectral features; Roman numerals I–IV mark RBs used to characterize the spectral types. PBS = Peña Blanca Spring, NC = Norton County.

were identified as moderately to heavily fragmented enstatite under crossed polarizers (Fig. 1a, bottom). One large pyroxene grain (confirmed by EPMA analyses; ~

0.5 cm along the long axis) is partly transformed or converted mainly in the inner part from enstatite into clinopyroxene, and it shows unusually high interference colors under crossed polarizers (Fig. 1a, insert).

The Norton County thin sections (Figs. 1b–d) show signs of abundant impact melting in the form of opaque melt veins. Mineral fragments are embedded in this melt as result of shock pressures exceeding ~ 60 GPa (Hörz and Cintala 1997). Some of the embedded grains or fragments in Norton County have a dark appearance indicating shock darkening by friction (Figs. 1b–d).

Based on the optical images, we focused in our study on five distinct components (areas; see Figs. 2a and 2b). Components of type [1] consist of large, single enstatite clasts (larger than 256×256 μm). A second component [2] shows a brecciated texture and is the fine-grained clastic matrix. A third analyzed component [3] represents the melt veins, recognizable as dark areas in the thin sections. Under a crossed polarizer, they reveal fine, needle-like crystals indicating quenching. As a fourth component [4], grains embedded in the melt vein were studied, and, finally, the last component consisted of shock-darkened areas of the fragments enclosed within the melt veins (Fig. 2b). These components with different appearances and textures are well distinguished in the in situ studies of the thin sections (Figs. 2a and 2b), while the bulk powder samples contain a mixture of all these minerals and components.

EMPA

Most analyzed grains (large clasts as well as grains within the brecciated areas) are pure Mg-endmembers of enstatite with a very low concentration of FeO (<0.1 wt% on average; Table 1). In addition to enstatite, diopside was present only as dissolution lamellae in enstatite. Accessory olivine occurs essentially as pure forsterite (Table 1).

The areas of the impact melt show a larger chemical variation, notably in that FeO is elevated when compared to the large grain analyses and averages (1.2–1.7 wt% on average), as well as 1.4–2.2 wt% CaO. Both SiO_2 (56.9–58.4 wt%) and MgO (37.8–39.5 wt%) in the melt areas are similar on average to the large enstatite clasts and the fine-grained brecciated enstatite-rich matrix (Table 1).

Diffuse Reflectance FTIR Bulk Powders

The diffuse reflectance spectra obtained from the powdered size fractions (Table 2; Fig. 3) show similar spectra for size fractions exceeding 25 μm. In the region from 8 to 18 μm, Peña Blanca Spring has several strong RBs, indicating a high crystallinity of the material. In

the region around 10 μm, the strongest feature is the RB at 10.4 μm. Further strong features are at 9 μm, 9.9 μm, and 11.6 μm. Several weaker bands fall between 8.8 μm and 11.1 μm. Further features are located at longer wavelengths at 13.8 μm, 14.4 μm, and 15.4 μm. The CF is at 8.1–8.4 μm. The CF is influenced by the bulk chemistry of the materials, for example, the SiO_2 composition. For the bulk powders, the CF falls clearly in the range observed for the minerals with the composition observed for this study (near 60 wt% SiO_2, Table 1; Cooper et al. 2002).

The finest grain size fraction (0–25 μm; Table 2) shows a distinct spectrum. The dominant feature is the TF at 12.7 μm, while the RBs have an overall lower intensity. Strong RBs within this size fraction are located at 9 μm, 9.3 μm, 9.9 μm, 10.4 μm, and 11.6 μm. Additional weaker features occur at 8.8 μm (shoulder) and 11.1 μm. Two bands at 14.1 μm and 14.8 μm are shifted compared with the corresponding RBs in the larger size fractions.

In all size fractions (Table 2), there are several features between 4 μm and 7.5 μm. In addition, there are absorbance features of volatiles at 2.8 μm, 3.4 μm, and 3.5 μm. In summary, the main difference in the powder spectra is that the band intensity decreases with decreasing grain sizes.

Micro-FTIR

Due to atmospheric interferences and sinusoidal features due to internal reflectance (e.g., Morlok et al. 2020), it is difficult to discern features in the spectral range below the CF (Morlok et al. 2016a,2016b; Table 3; Fig. 4), and these artifacts could also affect the exact determination of the CF. The micro-FTIR analyses were of spots with enstatite composition (Table 1) occurring in all textural settings, and, thus, the analyses share similar general spectral characteristics regarding their band positions.

However, there are significant differences in the spectra based on relative band intensities and the number of occurring RBs. This allows the spectra to be sorted or divided into four distinct spectral groups, which we subsequently refer to as types I–IV (Fig. 4). Mixtures of these different spectral types then make up the spectral signatures of the various components observed in the sample, as well as of the bulk powders.

Spectra of type I (Table 3; Fig. 4) are similar in band shapes and positions when compared to the bulk powder spectra and show the highest number of RBs. The CF is located between 8.3 μm and 8.6 μm. Three strong bands are at 9.0–9.3 μm, 10.3–10.6 μm, and 11.5–11.7 μm. Furthermore, weaker features are in the 8–12 μm region. There are stronger RBs at wavelengths

Table 1. EMPA analyses of mineral grains and melt areas (in wt%). Standard deviation (s.d.) is in 2 sigma. Representative analyses are used due to high homogeneity of the phases. Average of all spots are presented due to the heterogeneity of the glass. N.d. = not detected, b.d. = below detection limit (Mn: 0.04 wt%, Cr: 0.05 wt%, Na, K: 0.02 wt%, Fe: 0.04 wt%, Ti: 0.08 wt%).

| | Type I | | | | | |
Lithology	Single crystals	s.d.	Breccia	s.d.	Melt	s.d.
SiO_2	59.54	0.62	59.51	0.23	56.88	7.94
TiO_2	b.d.		b.d.		b.d.	
Al_2O_3	0.08	0.07	0.09	0.04	0.16	0.11
Cr_2O_3	b.d.		b.d.		0.10	0.06
FeO	b.d.		b.d.		1.48	0.49
MnO	0.05	0.07	0.06	0.07	b.d.	
MgO	40.02	0.65	40.04	0.66	39.47	9.10
CaO	0.38	0.30	0.45	0.19	1.42	1.23
Na_2O	b.d.		b.d.		0.07	0.10
K_2O	b.d.		b.d.		b.d	
Total	100.08		100.15		99.56	
N	21		5		18	

| | Type II | | | | | |
Lithology	Single crystals	s.d.	Breccia	s.d.	Melt	s.d.
SiO_2	59.45	0.41	59.48	0.24	56.85	4.13
TiO_2	b.d.		b.d.		b.d.	
Al_2O_3	0.07	0.05	0.07	0.05	0.23	0.15
Cr_2O_3	b.d.		b.d.		0.08	0.05
FeO	0.06	0.12	b.d.		1.65	0.78
MnO	0.06	0.10	0.08	0.08	b.d.	
MgO	39.98	0.70	40.06	0.55	38.56	3.23
CaO	0.40	0.47	0.35	0.31	2.21	0.66
Na_2O	b.d.		b.d.		0.09	0.06
K_2O	b.d.		n.d.		b.d.	
Total	100.03		100.03		99.66	
N	15		5		8	

| | Type III | | Type IV | | Diopside | | Olivine | |
Lithology	Single crystals	s.d.	Melt	s.d.	Single crystals	s.d.	Breccia	s.d.
SiO_2	59.62	0.03	58.35	2.26	55.67	0.62	55.87	0.16
TiO_2	b.d.		b.d.		0.17	0.21	0.15	0.07
Al_2O_3	0.10	0.10	0.29	0.43	0.42	0.34	0.50	0.06
Cr_2O_3	b.d.		0.07	0.08	b.d.		b.d.	
FeO	b.d.		1.24	1.35	b.d.		b.d.	
MnO	0.06	0.03	0.20	0.25	b.d.		0.05	0.04
MgO	40.20	0.37	37.80	5.08	20.27	0.71	20.50	1.35
CaO	0.35	0.80	1.91	2.08	23.58	0.83	22.81	1.20
Na_2O	b.d.	0.01	0.08	0.09	b.d.		0.31	0.12
K_2O	n.d.		b.d.		b.d.		b.d.	
Total	100.32		99.94		100.10		100.20	
N	2		5		8		3	

Table 2. Band positions for the grain size fractions of Peña Blanca Spring (in μm).

Grain size (in μm)																
0–25	2.30	2.83	2.94	3.38	3.40	3.48	4.95	5.34	5.54	5.92	6.12	6.25	6.52	6.71	6.92	7.01	7.13
25–63	2.30	2.83		3.38	3.41	3.48	4.95	5.34	5.54	5.92	6.12	6.25	6.52	6.72	6.92	7.01	7.13
63–125	2.30	2.83		3.38	3.41	3.48	4.95	5.34	5.54	5.92	6.13		6.53	6.71		7.02	7.13
125–250	2.31	2.83		3.38	3.41	3.48	4.95	5.34	5.53	5.92	6.13		6.52	6.70		7.00	7.12

Grain size (in μm)	CF										TF				
0–25	8.44	8.81	8.98	9.30	9.86		10.43		11.08	11.60	12.73	14.07		14.82	
25–63	8.39	8.82	9.00	9.27	9.86	10.19	10.38	10.75	11.07	11.56		13.82	14.40		15.43
63–125	8.36	8.83	8.99	9.28	9.86	10.20	10.39	10.74	11.07	11.56		13.83	14.41		15.42
125–250	8.14	8.81	8.99	9.27	9.86	10.19	10.38	10.75	11.07	11.57		13.83	14.41		15.42

CF: Christiansen feature, TF: transparency feature

Table 3. Band positions from micro-FTIR analyses of Peña Blanca Spring and Norton County (in μm). Always the range for a given band position is given: min = shortest wavelength, max = longest wavelength. Spectra are grouped into spectral types I–IV based on common spectral characteristics

	In μm	CF													
Type I	Min	8.31	8.69	8.95	9.36	9.53	9.85	10.00	10.13	10.31	10.51	10.73	11.02	11.54	
	Max	8.60	8.84	9.25	9.36	9.56	9.90	10.01	10.30	10.55	10.55	10.84	11.16	11.67	
Type II	Min	8.27		8.93		9.54	9.85	9.97	10.15	10.29		10.76	11.05	11.40	11.88
	Max	8.51		9.08		9.57	9.88	9.98	10.19	10.46		10.85	11.16	11.53	12.17
Type III	Min	8.44	8.89	9.15			9.88			10.39	10.54	10.76	11.25		
	Max	8.55	8.90	9.17			9.88			10.40	10.54	10.77	11.28		
Type IV	Min	7.91		9.14			9.81		10.17			10.84	11.06		11.88
	Max	7.98		9.17			9.94		10.18			10.89	11.08		11.91

	In μm														
Type I	Min	12.22	12.37		12.51	12.97	13.43	13.62	13.78		14.39	14.65	15.31
	Max	12.34	12.49		12.94	13.25	13.52	13.70	13.85		14.46	14.75	15.36
Type II	Min	12.19	12.36		12.53	12.78	13.43	13.62	13.78	13.89		14.34	14.50
	Max	12.34	12.47		12.63	13.28	13.47	13.63	13.85	14.17		14.45	14.80
Type III	Min		12.40	12.59		13.00			13.94				
	Max		12.40	12.59		13.00			13.94				
Type IV	Min								13.79				
	Max								13.79				

longer than 12 μm, at 13.8–13.9 μm, 14.4–14.5 μm (Fig. 4).

While exhibiting fewer bands than in the previous type I, spectra of type II are mostly similar in band positions to those of type I (Table 3; Fig. 4). Type II is characterized by a dominating RB at 8.9–9.1 μm, which is always the strongest feature. Weaker RBs are in the 11.4–11.5 μm range, which is clearly shifted when compared to equivalent RBs in type I (11.5–11.6 μm). The CF is at 8.3–8.5 μm, and further RBs are at 9.5–12.2 μm. More bands are located at longer wavelengths at 13.8–13.9 μm and 14.3–14.8 μm. Type II spectra lack

weaker RBs that do occur in type I spectra, namely in the range between 8.7 and 8.8 μm, at 9.4 μm, and at 10.5–10.6 μm.

Spectra of types III and IV consist of two spectra each and are characterized by only a few RB features. Type III (Table 3; Fig. 4) occurs in a large grain in Peña Blanca Spring and is characterized again by three equally strong RB at 9.2 μm, a double peak between 10.4 μm and 10.5 μm, and another strong RB at 11.3 μm. Further features are observed at 8.9 μm, 9.9 μm, and 10.8 μm. Weaker bands at longer

wavelengths are located at 12.4 μm, 12.6 μm, 13 μm, and 13.9 μm. The CF is clearly visible at 8.4–8.6 μm.

Spectra of type IV (Table 3; Fig. 4) are observed in the melt veins of Norton County characterized by a dominating strong RB between 10.8 μm and 11.1 μm, and a second characteristic strong RB at 9.1–9.2 μm. Additional weaker RBs are located in the 8–12 μm range, at 9.8–9.9 μm, 10.2 μm, and 11.9 μm. The CF is at 7.9–8 μm. A stronger band is located at longer wavelengths at 13.8 μm.

Spectral types I and II occur in all four mineralogical settings (large mineral clasts, clastic matrix, melt vein, fragments in melt vein), while spectral type III was only observed among the larger grains, and type IV in the melt veins.

DISCUSSION

Mineralogy of Bulk Powders and Type I–IV

The features observed in the bulk powder spectra are characteristic for enstatite-rich material, as enstatite is by far the dominant mineral phase in aubrites (Fig. 3). The comparison of our data with reference data of pure enstatite (Klima et al. 2007) and other Fe-poor (En$_{89-91}$) enstatite (Hamilton 2000) shows that for most features the literature data match the spectra obtained from Peña Blanca Spring samples in literature. The CF is located at 8.3 μm and significant RB features are at 8.7 μm, 8.8 μm, 8.9–9.0 μm, 9.1–9.5 μm, 9.9 μm, 10.2–10.3 μm, 10.4–10.5 μm, 10.9–11.1 μm, and 11.4–11.6 μm. The TF is at 12.7 μm. At longer wavelengths, there are RB in these enstatites at 13.5 μm, 14 μm, 14.8 μm, and 17.2 μm. There is only a weaker band at 13.5 μm that does not appear in our bulk powder results (Table 2) but does in the reference data. The similarity is also high for the overtone features and volatile bands at wavelengths shorter than the CF.

Among the micro-FTIR spectra, the situation is similar (Fig. 4). Spectra of type I show all significant enstatite features. The results for type II (Table 3) do not have the weak bands of the earlier studies (Hamilton 2000; Klima et al. 2007) at 8.7 μm and 8.8 μm in the reference enstatites. Compared with spectra of standard enstatite, spectra of type III (Table 3) lack bands at 8.7 μm, 10.2 μm, 11.1 μm, 12.6 μm, and 13.5 μm; this could be caused by the transformation from enstatite to clinopyroxene (Hamilton 2000; Klima et al. 2007).

The largest difference to the reference enstatite data is in the spectra of type IV (Table 3), which lack enstatite features at 8.7–9.0 μm, 10.4–10.5 μm, 11.4–11.6 μm, as well as at 13.5–14.8 μm (Hamilton 2000;

Klima et al. 2007). Type IV spectra correspond to areas within the melt veins in the Norton County aubrite. Rapid quenching and possible glass formation accounts for the apparent loss of crystallinity in this case related to impact events experienced by the aubrite parent body.

Comparison to Earlier Studies on Aubrites

In order to investigate the homogeneity of the bulk materials and validity of the results for general comparison purposes, we compare our bulk results with those of earlier mid-infrared studies of aubrites. These studies are of Peña Blanca Spring (Markus et al. 2018) and samples of Antarctic meteorite ALH78113 (Kimura et al. 1992).

The bulk powder spectra of Peña Blanca Spring are similar to those of earlier powder analyses for aubrites (Markus et al. 2018; Fig. 5). Two RELAB studies of the Antarctic finds ALH78113 (with grain size fractions of 0–45 μm and 45–125 μm) and of another Peña Blanca Spring sample (fraction < 90 μm) show strong RBs at 8.8–9 μm, 10.4 μm, and 11.5–11.6 μm (Markus et al. 2018), which is very similar to the results of bulk powdered Peña Blanca Spring in this study (Fig. 5). Weaker RBs located at 9.9 μm, 10.7 μm, and 11.1 μm in earlier studies also correspond well with our results. Only weak bands at 8.7 do not occur in our powder spectra.

The CF in the earlier analyses is located at 8.3–8.4 μm, which corresponds with results obtained in the results of this study (8.1–8.4 μm; Table 2) and is probably indicative of an overall similar bulk composition. The TF (at 12.7 μm in this study) is similar in most cases, but ranges from 12.1 μm to 12.8 μm. The shift can probably be explained by grain size differences between samples (Markus et al. 2018). Also in agreement with earlier studies are features at shorter wavelengths (below 8 μm), that is, volatile absorption features between 2.7 μm and 3.5 μm, and the overtone bands between 5 μm and 6.8 μm.

Relationships Between the Types (I–IV)

All spectra from types I–III were obtained from different areas dominantly comprised of enstatite as the main component. Types I and II spectra show effects related to crystal orientation (c-axis orientation), whereas spectra of types III and IV could show distinct features induced by shock metamorphism (Fig. 4).

In FTIR studies of oriented enstatites along the c-axis, a prominent RB (with regard to other RB intensities) was observed at 9.0–9.1 μm (Martin et al. 2018). This is similar to what we observe in type II
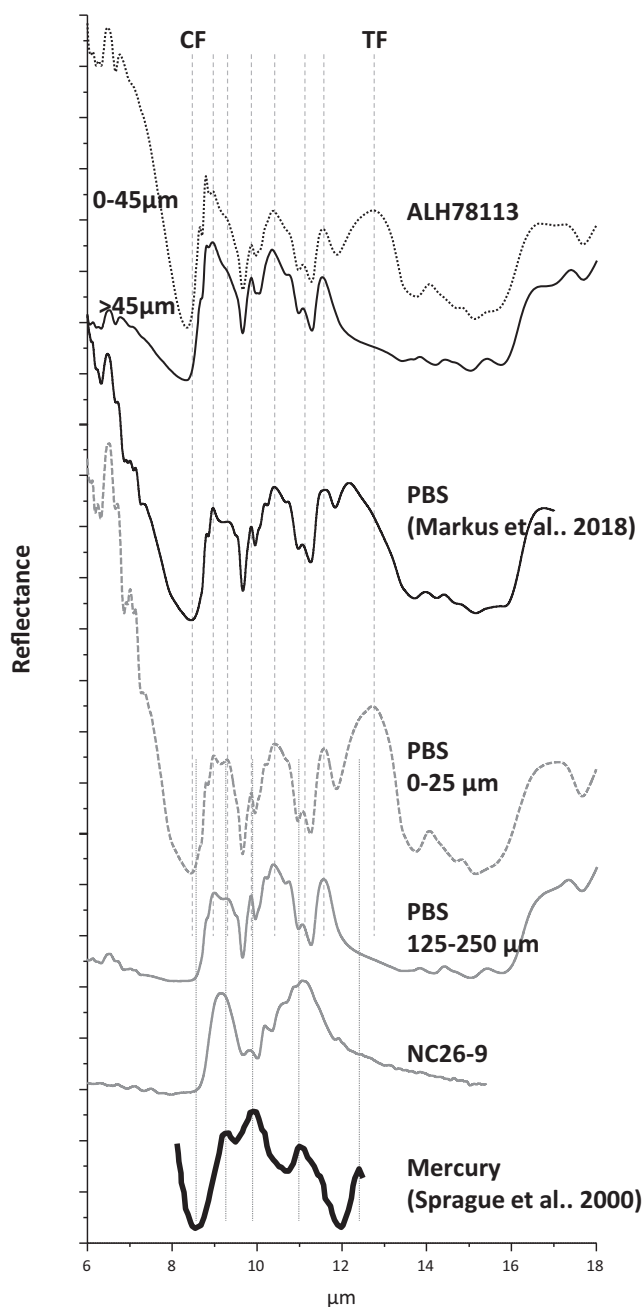
Fig. 5. PBS = Peña Blanca Spring, NC = Norton County, CF = Christiansen feature, TF = transparency feature. Top) Comparison of FTIR spectra from our study with data from earlier aubrite studies, ALH78113 and Peña Blanca Spring (Markus et al. 2018). Bottom) Ground-based astronomical spectrum of Mercury (Sprague et al. 2000). The gray spectra in the center are our results for Peña Blanca Spring size fractions, 0–25 μm (dotted line) and 125–250 μm (continuous line), and the micro-FTIR spectrum for group type IV spectra, that is, impact melt (NC26-9). The coarse dotted vertical lines are for the comparison of features with the bulk powder Peña Blanca Spring 0–25 μm spectrum, the finer dotted vertical lines for the comparison with the strongest features of the Mercury surface spectrum (Sprague et al. 2000).

spectra and is probably indicative of the aforementioned effects of crystal orientation. While band positions are similar for analyses along a- and b-axes, spectra along the c-axis show a significantly increased intensity for the 9.1 μm RB of over 80% compared to other RBs. Spectra of type I are similar to spectra of samples oriented along the a-axis (Martin et al. 2018).

Randomly oriented crystals, and mixtures of crystals and melt (as in the case of the fine-grained clastic matrix sample; Fig. 2a), explain the variations in relative band intensities among the types of spectra.

The sample related to type III spectra shows higher high interference colors under crossed polarizers (Fig. 1a, bottom), but it is still considered enstatite by our EMPA analyses. This loss of features compared to types I and II (Table 3; Fig. 4), and thus, the change in interference colors (Fig. 1a), could indicate incipient shock metamorphism. Alternatively, the change is due to the transformation from enstatite to clinopyroxene (Hamilton 2000; Klima et al. 2007). The very narrow chemistry especially in the large single crystals and breccia grains also supports orientation effects as main reason for the spectral variations of the same mineral enstatite in types I–III (Table 1).

Spectra of type IV are clearly different from the probable axis orientation spectra of types I and II and probably represent the potentially shock-affected enstatite single grain spectra that also comprise spectra of type III (Fig. 4). Type IV spectra contain fewer RBs compared to the types I–III spectra (Fig. 4). Type IV shows a prominent broad RB at ~11.1 μm (Table 3), falling into the "gap" between the two strong RBs of types I and III at ~10.3 μm and ~11.5 μm, which in turn do not appear as RBs at all in type IV spectra (Fig. 4; Table 3). While type II also has a significant RB at the 11.1 μm position, other RBs of type II are much weaker or nonexistent in type IV spectra (Table 3).

Analyses of type IV spectra were obtained from spots within the shock vein (Figs. 1b–d and 4), indicating that there is a variation in the degree of crystallization in the presumable melt veins, with possibly lower degrees of crystallites in the spots analyzed for type IV. However, the remaining prominent feature at 9.1–9.2 μm in type IV spectra (Table 3) shows that at least needle-like, skeletal crystal material is still left or newly formed in the material, or larger crystalline particles (Figs. 2c–f). An entirely quenched melt would show a spectrum dominated by only one strong band in the 10 μm region (e.g., Speck et al. 2011; Morlok et al. 2019).

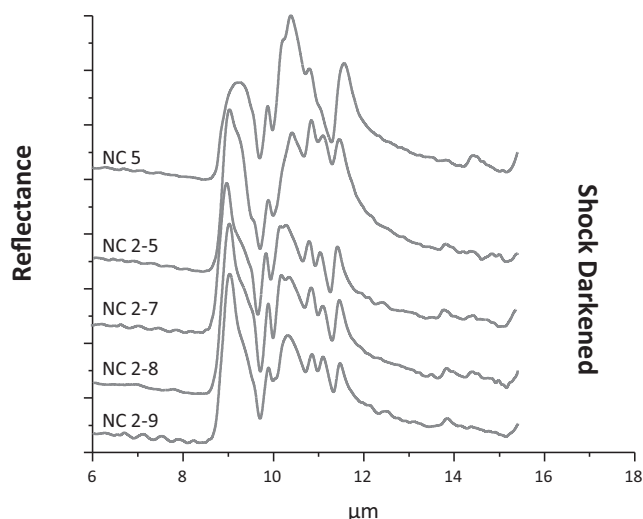This observation is similar to micro-FTIR spectra obtained from melt veins in the Chelyabinsk meteorite,

Fig. 6. Micro-FTIR spectra of presumably shock-darkened areas in fragments in Norton County. Four spectra are of type II, one from type I. NC = Norton County.

where melt veins show a similar relatively featureless spectrum. In comparison, unshocked and bulk material of Chelyabinsk shows more RBs, hinting at a higher degree of crystallinity (Morlok et al. 2017a).

In general, types I–IV spectra are based on similar spectral characteristics. Spectral types I and II occur in most components (large enstatite grains, fine-grained clastic matric, melt vein, shock darkened enstatite). Type III characteristics have only been found in one large mineral grain and spectral type IV features within spots of the melt vein.

Spectra of types I and II are found in the shock-darkened component (Fig. 6), with a dominance of the latter group. So no specific spectral characteristics, for example, based on shock effects for this group can be identified.

Comparison with Earlier IR Studies of Mercury

One of the goals of the spectral study of aubrites is the comparison with planetary surfaces, in particular with that of Mercury.

According to mid-infrared observations from Earth-based telescopes, the bulk surface of Mercury is mostly mafic and contains mainly plagioclase, pyroxene, and olivine (Sprague et al. 1994, 2000, 2002, 2007, 2009; Emery et al. 1998; Sprague and Roush 1998; Cooper et al. 2001; Donaldson-Hanna et al. 2007). Thus, we are also compare our spectral results with a spectrum obtained by the Mid-Infrared Array Camera (MIRA) at the Kitt Peak Observatory from a Hermean surface portion at approximately 210–250° longitude that has a high signal-to-noise ratio (Sprague et al. 2000; Fig. 5).

The spectrum, recalculated from emissivity and baselined to reflectance, has strong RBs at 9.3 μm, 9.9 μm, and 11.0 μm. The CF is at 8.5 μm, and a (potential) TF is at 12.4 μm (Sprague et al. 2000).

The material that fit best, as determined Sprague et al. (2000), was ultramafic picrite or sodalithe-rich material.

In direct comparison, the spectra obtained in our study from Peña Blanca Spring bulk powder samples have a comparable CF from 8.1 μm to 8.4 μm and similar RBs at 9.3 μm, 9.9 μm, and 11.1 μm (Table 2). The TF in our analyses is at 12.7 μm (Table 2). In addition, the 9.9 μm band is a dominating feature in the astronomical spectrum but only a minor feature in the aubrite data, similar to the 11.1 μm feature (Table 2). Furthermore, the Mercury spectrum is lacking several bands visible in the laboratory spectrum at 9.0 μm, and especially the strong features at 10.4 μm and 11.6 μm (Table 2).

Type IV spectra from this study, which are associated with impact melt component, show a similarity to the Hermean surface: Two strong RBs at 9.1–9.2 μm and 11.1 μm have equivalents in the Mercury spectrum (Table 3), whereas a weaker feature is located at the position of the prominent 9.9 μm band. The CF is a slightly shifted in the melt spectra, at 7.9–8 μm compared to 8.5 μm for the Hermean surface (Table 3).

Finally, an important factor that has to be taken into account in spectral studies of surfaces of atmosphere less bodies is space weathering. Mercury can be expected to be severely affected by radiation and particles from the near sun, thus altering the properties of a thin surface layer (amorphization, plus formation of nanophase iron or graphite). Graphite and metal do not feature vibrational features in the spectral region of interest (Baldridge et al. 2009; Meerdink et al. 2019).

Amorphization probably results in the weakening of the silicate features (e.g., Weber et al. 2020).

SUMMARY AND CONCLUSIONS

Spectral features are similar in the bulk powder and micro-FTIR studies for both aubrites, Peña Blanca Spring and Norton County. Apart from the "mainstream" enstatite RBs identified in both aubrites, we were able to assign four peculiar enstatite spectral types based on micro-FTIR studies. Spectral types I and II probably display axis orientation-related dependencies of their respective enstatite-typical RBs, and type III spectra may show signs of incipient modifications due to shock metamorphism. The spectral peculiarities of type IV spectra seem to be related to the content of melt glass among crystallites in a quenched melt of the Norton County aubrite.

Components or textural areas identified in the two meteorites are unevenly distributed among the samples. So a strong difference at least between larger fragments of Norton County may exist. Larger parts are either dominated by melt veins and embedded grains (components 3 and 4; Figs. 1b and 1c), or others entirely by solid grains or breccia (Figs 1b and 1d). Peña Blanca Spring in our study only shows the larger grains in finer brecciated material (components 1 and 2). While a representative modal abundance is difficult based only on a couple of thin sections, the variations already visible on such few samples may reflect the occurrence of larger parts with similar compositions on the aubrite parent body. So the bulk powder spectra would only tell a part of the story, and hide signatures of components (or lithologies) of which the in situ micro-FTIR infrared spectra would be representative.

Bulk powder results in this study are very similar to previous spectral studies of aubrites (e.g., Markus et al. 2018), indicating that aubrites share general properties and the spectra are representative for this type of meteorite.

Regarding similarity to the spectral properties of the Hermean surface, the RBs—indicative of crystalline enstatite, especially the 10.4 μm band prominent in the bulk powder spectra (Fig. 4)—do not yield a suitable fit with the Hermean surface data (Sprague et al. 2000). Sprague et al. (2000) name augite, bronzite, plagioclase, and fayalite as possible candidates for the ~11 μm RB in the bulk spectrum of Mercury, but, except for plagioclase, the other candidates can be dismissed due to now available surface chemical data of Mercury (Namur and Charlier 2017; Vander Kaaden et al. 2017).

Therefore, enstatite-rich meteorites such as aubrites as source of a major constituent of Mercury's crust seem highly unlikely. Only the type IV-related spectra, which are associated with quenched impact glass sites, are more consistent with currently available Mercury data (and here especially the ~11 μm RB; Fig. 5) (e.g., Morlok et al. 2017a, 2017b).

In addition, recent studies based on MESSENGER results indicate compositional heterogeneity across the surface of Mercury (Nittler et al. 2011; Namur and Charlier 2017; Vander Kaaden et al. 2017).

While most regolith mineralogical compositions from Vander Kaaden et al. (2017) require substantial feldspar as component in the modeled surface regions, enstatite contents of only up to 37% were modeled. Experimental studies by Namur and Charlier (2017) also allow for the presence of a substantial abundance of enstatite (up to 20%) in addition to abundant glass. While this would allow for aubrite-type material in these material mixtures, especially a melt-like component like lithology type IV, such a component is not a fundamental requirement.

Also, in the spectra of remote sensing data of planetary surfaces such as Mercury with MERTIS, we probably will always see mixtures of several phases (analogous to the bulk powder studies). So the identification of the amorphous, shock affected material will be clearly possible if it is a dominant component in the observed area. If not, we have to take the features of additional, crystalline material into account which will make an unambiguous characterization difficult.

Editorial Handling—Dr. Edward Cloutis

REFERENCES

Armstrong J. T. 1991. Quantitative elemental analysis of individual microparticles with electron beam instruments. In *Electron probe quantitation*, edited by Heinrich K. F. J. and Newbury D. E. New York: Plenum Press. pp. 261–315.

Baldridge A. M., Hook S. J., Grove C. I., and Rivera G. 2009. The ASTER spectral library version 2.0. *Remote Sensing of Environment* 113:711–715.

Barrat J. A., Greenwood R. C., Keil K., Rouget M. L., Boesenberg J. S., Zanda B., and Franchi I. A. 2016. The origin of aubrites: Evidence from lithophile trace element abundances and oxygen isotope compositions. *Geochimica et Cosmochimica Acta* 192:29–48.

Benkhoff J., van Casteren J., Hayakawa H., Fujimoto M., Laakso H., Novara M., Ferri P., Middleton H. R., and Ziethe R. 2010. BepiColombo–-Comprehensive exploration of Mercury: Mission overview and science goals. *Planetary and Space Science* 58:2–20.

Blewett D. T. and Burbine T. H. 2007. Angrites as samples of Mercury? A spectral perspective (abstract #1203) 38th Lunar and Planetary Science Conference. CD-ROM.

Burbine T. H., McCoy T. J., Nittler L. R., Benedix G. K., Cloutis E. A., and Dickinson T. L. 2002. Spectra of extremely reduced assemblages: Implications for Mercury. *Meteoritics & Planetary Science* 37:1233–1244.

Christensen P. R., Bandfield J. L., and Hamilton V. E. 2001. Mars global surveyor thermal emission spectrometer experiment: Investigation description and surface science results. *Journal of Geophysical Research* 106:23,823–23,872.

Clarke R. N. 1999. Spectroscopy of rocks and minerals, and principles of spectroscopy. In *Remote sensing for the Earth sciences: Manual of remote sensing*, 3rd ed., edited by Rencz A. N. New York: John Wiley & Sons.

Cloutis E. A. and Gaffey M. J. 1993. Accessory phases in aubrites: Spectral properties and implications for asteriod 44 NYSA. *Earth, Moon, and Planets* 63:227–243.

Cloutis E. A., Gaffey M. J., and Applin D. M. 2016. Spectral reflectance properties of aubrites (abstract #1903) 47th Lunar and Planetary Science Conference. CD-ROM.

Cooper B., Potter A., Killen R., and Morgan T. 2001. Midinfrared spectra of Mercury. *Journal of Geophysical Research* 106:32803–32814.

Cooper B. L., Salisbury J. W., Killen R. M., and Potter A. E. 2002. Midinfrared spectral features of rocks and their powders. *Journal of Geophysical Research* 107:5017–5034.

Donaldson-Hanna K. L., Sprague A. L., Kozlowski R. W. H., Boccafolo I., and Warell J. 2007. Mercury and the Moon: Initial findings from mid-infrared spectroscopic measurements of the surface (abstract #2291) 38th Lunar and Planetary Science Conference Abstract.

Donaldson Hanna K. L., Thomas I. R., Bowles N. E., Greenhagen B. T., Pieters C. M., Mustard J. F., Jackson C. R. M., and Wyatt M. B. 2012. Laboratory emissivity measurements of the plagioclase solid solution series under varying environmental conditions. *Journal of Geophysical Research* 117:E11004.

Emery J. P., Sprague A. L., Witteborn F. C., Colwell F. C., and Kozlowski R. W. H. 1998. Mercury: Thermal modeling and mid-infrared (5–12 μm) observations. *Icarus* 136:104–123.

Ferrari S., Maturilli A., Carli C., D'Amore M., Jörn H., Nestola F., and Hiesinger H. 2020. Thermal infrared emissivity of felsic-rich to mafic-rich analogues of hot planetary regoliths. *Earth and Planetary Science Letters* 534:116089.

Gladman B. and Coffey J. 2007. Mercurian impact ejecta: Meteorites and mantle. *Meteoritics & Planetary Science* 44:285–291.

Hamilton V. E. 2000. Thermal infrared emission spectroscopy of the pyroxene mineral series. *Journal of Geophysical Research* 105:9701–9716.

Hapke B. 1993. *Theory of reflectance and emittance spectroscopy*. New York: Cambridge University Press.

Helbert J., Moroz L. V., Maturilli A., Bischoff A., Warell J., Sprague A., and Palomba E. 2007. A set of laboratory analogue materials for the MERTIS instrument on the ESA BepiColombo mission to Mercury. *Advances in Space Research* 40:272–279.

Helbert J., Nestola F., Ferrari S., Maturilli A., Massironi M., Redhammer G. J., Capria M. T., Carli C., Capaccioni F., and Bruno M. 2013. Olivine thermal emissivity under extreme temperature ranges: Implication for Mercury surface. *Earth and Planetary Science Letters* 371:252–257.

Hiesinger H., Helbert J., and Mertis Co-I Team. 2010. The Mercury radiometer and thermal infrared spectrometer (MERTIS) for the BepiColombo mission. *Planetary and Space Science* 58:144–165.

Hörz F. and Cintala M. 1997. Impact experiments related to the evolution of planetary Regoliths. *Meteoritics & Planetary Science* 32:179–209.

Izawa M. R. M., Applin D. M., Mann P., Craig M. A., Cloutis E. A., Helbert J., and Maturilli A. 2013. Reflectance spectroscopy (200–2500 nm) of highly-reduced phases under oxygen- and water-free conditions. *Icarus* 226:1612–1617.

Kimura M., Lin Y.-T., Ikeda Y., El Goresy A., Yanai K., and Kojima H. 1992. Petrology and mineralogy of Antarctic aubrites, Y-793592 and ALH-78113, in comparison with non-Antarctic aubrites and E-chondrites. Antarctic Meteorites XVII. Papers presented to the 17th Symposium on Antarctic Meteorites, NIPR, Tokyo, August 19–21.

King P. I., McMillan P. F., and Moore G. M. 2004. Infrared spectroscopy of silicate glasses with application to natural systems. In *Infrared spectroscopy in geochemistry, exploration geochemistry, and remote sensing*, Mineral, Assoc. of Can. Short Course, vol. 33, edited by King P. L., Ramsey M. S., and Swayze G. A. Ottawa: Mineralogical Association of Canada. pp. 93–133.

Klima R. L., Pieters C. M., Sunshine J. M., Hiroi T., Bishop J. L., Lane M. D., Dyar M. D., and Treiman A. H. 2007. Coordinated spectroscopic and petrologic investigation of LAP 04840: First results of infrared, thermal and Raman spectroscopy. *Meteoritics & Planetary Science* 42:235–253.

Kuehner S. M. and Irving A. J. 2007. Grain boundary glasses in the plutonic angrite NWA 4590: Evidence for rapid decompressive partial melting and cooling on Mercury? (abstract #1522) 38th Lunar and Planetary Science Conference. CD-ROM.

Lodders K., Palme H., and Wlotzka F. 1993. Trace elements in mineral separates of the Pena Blanca Spring aubrite: Implications for the evolution of the aubrite parent body. *Meteoritics* 28:538.

Lonsdale J. T. 1947. The Peña Blanca Spring meteorite, Brewster County, Texas. *American Mineralogist* 32:354–364.

Love S. G. and Keil K. 1995. Recognizing Mercurian meteorites. *Meteoritics* 30:269.

Markus K., Moroz L., Arnold G., Henckel D., Hiesinger H., Rohrbach A., and Klemme S. 2018. Reflectance spectra of synthetic Fe-free ortho- and clinoenstatites in the UV/VIS/IR and implications for remote sensing detection of Fe-free pyroxenes on planetary surfaces. *Planetary and Space Science* 159:43–55.

Martin D. J. P., Leiva A., Bell S. K., Pernet-Fisher J. F., Joy K. H., Morlok A., Wogelius R. A., and Hiesinger H. 2018. Investigating the orientation of minerals using FTIR microspectroscopy (abstract #2083) 49th Lunar and Planetary Science Conference. CD-ROM.

McCoy T. J. and Bullock E. S. 2015. Volatile-rich phases in aubrites: Clues to understanding the mineralogy of mercury? (abstract # 1856) 78th Annual Meeting of the Meteoritical Society.

McCubbin F. M., Vander Kaaden K. E., Peplowski P. N., Bell A. S., Nittler L. R., Boyce J. W., Evans L. G., Keller L. P., Elardo S. M., and McCoy T. J. 2017. A low O/Si ratio on the surface of mercury: Evidence for silicon smelting? *Journal of Geophysical Research: Planets* 122:2053–2076.

Meerdink S. K., Hook S. J., Roberts D. A., and Abbott E. A. 2019. The ECOSTRESS spectral library version 1.0. *Remote Sensing of Environment* 230:1–8.

Mittlefehldt D. W., McCoy T. J., Goodrich C. A., and Kracher A. 1998. Non-chondritic meteorites from asteroidal bodies. In *Planetary materials*, edited by Papike J. J. Washington, District of Columbia: The Mineralogical Society of America. pp. 195–233.

Morlok A., Koike C., Tomeoka K., Mason A., Lisse C., Anand M., and Grady M. 2012. Mid-infrared spectra of differentiated meteorites (achondrites): Comparison with astronomical observations of dust in protoplanetary and debris disks. *Icarus* 219:48–56.

Morlok A., Mason A. B., Anand M., Lisse C. M., Bullock E. S., and Grady M. M. 2014. Dust from collisions: A way to probe the composition of exo-planets? *Icarus* 239:1–14.

Morlok A., Stojic A. N., Dittmar I., Hiesinger H., Tiedeken M., Sohn M., Weber I., and Helbert J. 2016a. Mid-infrared spectroscopy of impactites from the Nördlinger Ries impact crater. *Icarus* 264:352–368.

Morlok A., Stojic A. N., Weber I., Hiesinger H., Zanetti M., and Helbert J. 2016b. Mid-infrared bi-directional reflectance spectroscopy of impact melt glasses and tektites. *Icarus* 278:162–179.

Morlok A., Bischoff A., Patzek M., Sohn M., and Hiesinger H. 2017a. Chelyabinsk —A rock with many different (stony) faces: An infrared study. *Icarus* 284:431–442.

Morlok A., Klemme S., Weber I., Stojic A. N., Sohn M., and Hiesinger H. 2017b. IR spectroscopy of synthetic glasses with Mercury surface composition: Analogs for remote sensing. *Icarus* 296:123–138.

Morlok A., Klemme S., Weber I., Stojic A. N., Sohn M., Hiesinger H., and Helbert J. 2019. Mid-infrared spectroscopy of planetary analogs: A database for planetary remote sensing. *Icarus* 324:86–103.

Morlok A., Hamann C., Martin D., Weber I., Joy K. H., Hiesinger H., Wogelius R., Stojic A. N., and Helbert J. 2020. Mid-infrared spectroscopy of laser-produced basalt melts for remote sensing application. *Icarus* 335:113410.

Moroz L. V. and Schade U. 2011. Effects of viewing geometry on thermal infrared spectra of planetary surfaces: The case of enstatite. EPSC-DPS Joint Meeting 2011, Abstract 1098.

Mustard J. F. and Hays J. E. 1997. Effects of hyperfine particles on reflectance spectra from 0.3 to 25 μm. *Icarus* 125:145–163.

Namur O. and Charlier B. 2017. Silicate mineralogy at the surface of Mercury. *Nature Geoscience* 10:9–13.

Namur O., Collinet M., Charlier B., Grove T. L., Holtz F., and McCammon C. 2016. Melting processes and mantle sources of lavas on Mercury. *Earth and Planetary Science Letters* 439:117–128.

Nicodemus F. E. 1965. Directional reflectance and emissivity of an opaque surface. *Applied Optics* 4:767–773.

Nittler L. R., Starr R. D., Weider S. Z., McCoy T. J., Boynton W. V., Ebel D. S., Ernst C. M., Evans L. G., Goldsten J. O., Hamara D. K., Lawrence D. J., McNutt R. L., Schlemm C. E., Solomon S. C., and Sprague A. L. 2011. The major-element composition of Mercury's surface from MESSENGER X-ray spectrometry. *Science* 333:1847–1849.

Okada A. and Keil K. 1981. Caswellsilverite, NaCrS2, a new mineral in the Norton County enstatite achondrite. *Meteoritics* 16:370.

Okada A., Keil K., Taylor G. J., and Newsom H. 1988. Igneous history of the aubrite parent asteroid: Evidence from the Norton County enstatite achondrite. *Meteoritics* 23:59.

Rothery D. A., Massironi M., Alemanno G., Barraud O., Besse S., Bott N., Brunetto R., Bunce E., Byrne P., Capaccioni F., Capria M. T., Carli C., Charlier B., Cornet T., Cremonese G., D'Amore M., De Sanctis M. C., Doresoundiram A., Ferranti L., Filacchione G., Galluzzi V., Giacomini L., Grande M., Guzzetta L. G., Helbert J., Heyner D., Hiesinger H., Hussmann H., Hyodo R., Kohout T., Kozyrev A., Litvak M., Lucchetti A., Malakhov A., Malliband C., Mancinelli P., Martikainen J., Martindale A., Maturilli A., Milillo A., Mitrofanov I., Mokrousov M., Morlok A., Muinonen K., Namur O., Owens A., Nittler L. R., Oliveira J. S., Palumbo P., Pajola M., Pegg D. L., Penttilä A., Politi R., Quarati F., Re C., Sanin A., Schulz R., Stangarone C., Stojic A., Tretiyakov V., Väisänen T., Varatharajan I., Weber I., Wright J., Wurz P., and Zambon F. 2020. Rationale for BepiColombo studies of Mercury's surface and composition. *Space Science Reviews* 216:66.

Salisbury J. W. 1993. Mid-infrared spectroscopy: Laboratory data. In *Remote geochemical analysis: Elemental and mineralogical composition*, edited by Pieters C. M. and Englert P. A. J. Cambridge, UK: Cambridge University Press.

Salisbury J. W. and Wald A. 1992. The role of volume scattering in reducing spectral contrast of reststrahlen bands in spectra of powdered minerals. *Icarus* 96:121–128.

Salisbury J. W., Walter L. S., Vergo N., and D'Aria D. M. 1991. *Infrared (2.1–25 μm) spectra of minerals*. Baltimore, Maryland: Johns Hopkins University Press.

Sandford S. A. 1984. Infrared transmission spectra from 2.5 to 25 μm of various meteorite classes. *Icarus* 60:115–126.

Speck A. K., Whittington A. G., and Hofmeister A. M. 2011. Disordered silicates in space: A study of laboratory spectra of 'amorphous' silicates. *Astrophysical Journal* 740:93–110.

Sprague A. L. and Roush T. L. 1998. Comparison of laboratory emission spectra with Mercury telescopic data. *Icarus* 133:174–183.

Sprague A. L., Kozlowski R. W. H., Witteborn F. C., Cruikshank D. P., and Wooden D. H. 1994. Mercury: Evidence for anorthosite and basalt from mid-infrared (7.5-13.5 micrometer) spectroscopy. *Icarus* 109:156–167.

Sprague A., Deutsch L. K., Hora J., Fazio G. G., Ludwig B., Emery J., and Hoffmann W. F. 2000. Mid-infrared (8.1–12.5 μm) imaging of Mercury. *Icarus* 147:421–432.

Sprague A. L., Emery J. P., Donaldson K. L., Russell R. W., Lynch D. K., and Mazuk A. L. 2002. Mercury: Mid-infrared (3–13.5 μm) observations show heterogeneous composition, presence of intermediate and basic soil types, and pyroxene. *Meteoritics & Planetary Science* 37:1255–1268.

Sprague A., Warell J. M., Cremonese G., Langevin Y., Helbert J., Wurz P., Veselovsky I., Orsini S., and Milillo A. 2007. Mercury's surface composition and character as measured by ground-based observations. *Space Science Reviews* 132:399–431.

Sprague A. L., Donaldson Hanna K. L., Kozlowski R. W. H., Helbert J., Maturilli A., Warell J. B., and Hora J. L. 2009. Spectral emissivity measurements of Mercury's surface indicate Mg- and Ca-rich mineralogy, K-spar, Na-rich plagioclase, rutile, with possible perovskite, and garnet. *Planetary and Space Science* 57:364–383.

Thomson J. L. and Salisbury J. W. 1993. The mid-infrared reflectance of mineral mixtures 7–14 microns. *Remote Sensing of Environment* 45:1–13.

Udry A., Wilbur Z. E., Rahib R. R., McCubbin F. M., Vander Kaaden K., McCoy T. J., Ziegler K., Gross J., DeFelice C., Combs L., and Turrin B. D. 2019. Reclassification of four aubrites as enstatite chondrite impact melts: Potential geochemical analogs for Mercury. *Meteoritics & Planetary Science* 54:785–810.

Vander Kaaden K. E., McCubbin F. M., Nittler L. R., Peplowski P. N., Weider S. Z., Frank E. A., and McCoy T. 2017. Geochemistry, mineralogy, and petrology of boninitic and komatiitic rocks on the Mercurian surface: Insights into the Mercurian mantle. *Icarus* 285:155–168.

Vaughan W. M. and Head J. W. 2014. Criteria for identifying Mercurian meteorites (abstract #1777) 45th Lunar and Planetary Science Conference. CD-ROM.

Warrell J., Sprague A., Kozlowski R., Rothery R. A., Lewis N., Helbert J., and Cloutis E. 2010. Constraints on Mercury's surface composition from MESSENGER and ground-based spectroscopy. *Icarus* 209:138–163.

Watters T. R. and Prinz M. 1979. Aubrites: Their origin and relationship to enstatite chondrites. Proceedings, 10th Lunar and Planetary Science Conference. pp. 1073–1093.

Weber I., Morlok A., Bischoff A., Hiesinger H., Ward D., Joy K. H., Crowther S. A., Jastrzebski N. D., Gilmour J. D., Clay P. L., Wogelius R. A., Greenwood R. C., Franchi I. A., and Münker C. 2016. Cosmochemical and spectroscopic properties of Northwest Africa 7325—A consortium study. *Meteoritics & Planetary Science* 51:3–30.

Weber I., Stojic A. N., Morlok A., Reitze M. P., Markus K., Hiesinger H., Pavlov S. G., Wirth R., Schreiber A., Sohn M., Hübers H.-W., and Helbert J. 2020. Space weathering by simulated micrometeorite bombardment on natural olivine and pyroxene: A coordinated IR and TEM study. *Earth and Planetary Science Letters* 530:115884.

Weider S. Z., Nittler L. R., Starr R. D., McCoy T. J., Stockstill-Cahill K. R., Byrne P. K., Denevi B. W., Head J. W., and Solomon S. C. 2012. Chemical heterogeneity on Mercury's surface revealed by the MESSENGER X-Ray Spectrometer. *Journal of Geophysical Research* 117:CiteID E00L05.

Weider S. Z., Nittler L. R., Starr R. D., Crapster-Pregont E. J., Peplowski P. N., Denevi B. W., Head J. W., Byrne P. K., Hauck S. A., Ebel D. S., and Solomon S. C. 2015. Evidence for geochemical terranes on Mercury: Global mapping of major elements with MESSENGER's X-Ray Spectrometer. *Earth and Planetary Science Letters* 416:109–120.

Zolotov M. Y., Sprague A. L., Hauck S. A., Nittler L. R., Solomon S. C., and Weider S. Z. 2013. The redox state, FeO content, and origin of sulfur-rich magmas on Mercury. *Journal of Geophysical Research: Planets* 118:138–146.